Comparison of high resolution pressure measurements on a high-rise building in a closed and open-section wind tunnel

Giacomo Lamberti[a,*], Luca Amerio[b], Giulia Pomaranzi[c], Alberto Zasso[c], Catherine Gorlé[a]

[a] *Stanford University, Y2E2 Building, 473 Via Ortega, Stanford, CA, 94305*
[b] *Advanced Technology + Research group, ARUP, UK*
[c] *Politecnico di Milano, Via G. La Masa 1, 20156, Milan, Italy*

Abstract

Wind tunnel testing represents an established technique for the assessment of wind-induced pressure on cladding systems. Nonetheless, some physical events, such as the pressure peaks that occur on a building's lateral facades, are not fully understood. To enable detailed analysis of the nature of these pressure peaks, we performed high-resolution pressure measurements on a high-rise building in two different wind tunnels: the closed-circuit wind tunnel of Politecnico di Milano, and the open-circuit Wall of Wind facility at Florida International University. The objective of the paper is to present the experimental set-up and the high-resolution pressure data, and to investigate the characteristics of the extreme suction events at individual pressure taps and their relevance for cladding design. We first compare the two atmospheric boundary layers, and subsequently present the pressure coefficients statistics. Then, we present probability density functions of the local and area-averaged pressure coefficients and visualize the space-time characteristics of two peak events to investigate their relevance for cladding design. The experiments provide consistent results and exhibit two types of suction events: one is characterized by an extremely short duration and spatial extension, while the other impacts a larger portion of the facade.

Keywords: wind tunnel, cladding, atmospheric boundary layer, pressure peaks

*Corresponding author
Email addresses: giacomol@stanford.edu (Giacomo Lamberti), gorle@stanford.edu (Catherine Gorlé)

1. Introduction

For the design of cladding, such as the glazed panels often employed to cover high-rise building facades, the correct estimation of wind loads is critical, both from a safety and economic point of view. Building codes provide different approaches to estimate the pressure acting on the panels but when the pressure-induced load is critical, common practice is to rely on wind tunnel cladding tests. During such experiments, pressure time-series are recorded in several points on the building's surface by means of a synchronous multi-pressure sensing system (SMPSS) [1–8]. On a building's lateral facades these pressure time series often exhibit extreme suction events. In these regions, the pressure is characterized by strong non-Gaussian behavior [9–15]; pressure peaks that correspond to pressure coefficients lower than -10 have been observed and result in large negative skewness [16, 17]. The spatial characteristics of these pressure peaks are still not fully understood and pose a challenge for dimensioning the cladding system: strong suction events that are extremely localized might not be relevant for cladding design, while events that extend over a larger region could play an important role.

Previous studies on the spatial distribution of pressure peaks have focused primarily on low-rise buildings [18–23]. To enable detailed analysis of these peak events on high-rise buildings, we performed high-resolution pressure measurements in two different wind tunnels. The first experiment was performed in the atmospheric boundary layer (ABL) wind tunnel of the Politecnico di Milano (PoliMi). It focused on measuring the pressure in the most critical regions on a high-rise building faade, i.e. adjacent to the corners and edges of the side walls, for an open-terrain exposure and different inflow directions. To enable analysis of the temporal and spatial extension of the peak events, the model was equipped with 447 closely-spaced pressure taps connected to high-frequency pressure scanners [17].

The same high-rise building model was then tested at the Wall of Wind (WoW) facility of Florida International University.The objective of this second round of tests was to verify if the spatial and temporal characteristics of the pressure peak phenomena observed in the PoliMi experiment could be reproduced in the WoW. Hence, the tests were performed using a similar open-terrain exposure, considering a subset of critical inflow directions identified at PoliMi [17]. To promote the dissemination of the data as a benchmark test case for the determination of wind loading on high-rise buildings, the PoliMi dataset is available to the scientific community on the open-access repository Zenodo [24], while the WoW dataset is available on the Stanford digital repository (SDR, [25]).

The objective of this paper is to present the experimental set-up and the high-resolution pressure data, and to investigate the characteristics of the extreme suction events at individual pressure taps and their effect on the area-averaged pressure of glazed panels. In the following, we first discuss the experimental set-up in both wind tunnels, considering the velocity measurements performed to characterize the ABL, and the pressure measurements on the high-rise building. Subsequently, we present the comparison of the results. To verify the consistency of the two incoming ABLs, we compare the profiles of mean velocity, turbulence intensity, integral time-scales and spectra. The wind pressure measurements are first compared in terms of the mean, root mean square, and spectra of the pressure coefficients. Subsequently we present pressure coefficient time-series to determine the frequency and intensity of the pressure peaks, together with probability density functions of local and area-averaged pressure coefficients. To interpret these results, additional visualization of the spatial and temporal extent of individual peak events, and of their effect on the area-averaged pressure on a cladding element, is performed. Finally, extreme value analysis is used to compute the peak pressure coefficient on individual taps and the design pressure coefficient for a typical glazed panel. The last section of the paper summarizes the conclusions and possible areas of future research.

2. Experimental setup

The PoliMi facility is a closed-circuit wind tunnel; the boundary layer test section has a cross section of 14×4 m^2 and is 35m long. The models are placed at a distance of 10m from the inlet, in the center of a turntable of radius 6.5m, to enable tests at different wind directions. The WoW ABL facility is an open-circuit wind tunnel with a 6.1m wide and 4.3m high test section, and a turntable with a radius of 4.9m. In the following, we first describe the set-up of the velocity measurements, performed at the center of the turntable in absence of the model to characterize the ABL in both wind tunnels. Subsequently we introduce the set-up for the pressure measurements on the high-rise building.

2.1. Velocity measurements

In the PoliMi wind tunnel, a detailed characterization of the ABL was carried out using 3D hot-wires with a sampling frequency of 2000Hz. The velocity components were measured at 280 points distributed on a plane at the building location, as shown in Figure 1. The outcome of the experiment consists of 20s time-series of the three velocity components at 5 spanwise locations (0.6m apart) and 56 vertical locations (43.7mm apart below 0.75m and 87.5mm apart above).

(a) Setup of the experiment to characterize the ABL at PoliMi

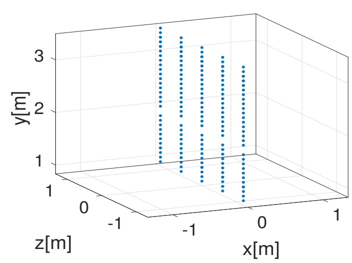

(b) Coordinates of the hot-wire measurements

Figure 1: PoliMi experimental setup of velocity measurements.

The ABL in the WoW was characterized using TFI Cobra probes with a sampling frequency of 2500Hz. 60s time-series of the three components of velocity were recorded at 6 vertical locations in the center of the turntable. The spatial resolution of these measurements varied between 0.3m and 0.6m. Table 1 summarizes the parameters of the two experiments in terms of sampling frequency, total duration, and reference velocity at 2m height. The WoW tests were run at a higher reference velocity than the PoliMi tests; the comparisons in section 3.1 will be presented in terms of non-dimensional quantities.

	$f_{samp}[Hz]$	$T[s]$	$U_{ref}[m/s]$
PoliMi	2000	20	7.8
WoW	2500	60	35.4

Table 1: Sampling frequency, total duration, and reference velocity at 2m height for the velocity measurements performed in both facilities.

2.2. Pressure measurements

2.2.1. Building model

The same high-rise building model was used in both experimental facilities. It is a 1m wide, 0.3m deep and 2m high rectangular box, representative of a 100m tall building in full-scale. The model was placed at the center of a turntable to allow testing at different inflow directions. In the present work we focus on three wind directions: 0°, 20° and 180°, following the convention defined in Figure 2. Results for the 0° and 180° tests have been previously presented in [26]; in this paper we add the analysis for the downwind wind direction of 20°, since strong peak suction events have been observed for this wind direction [17].

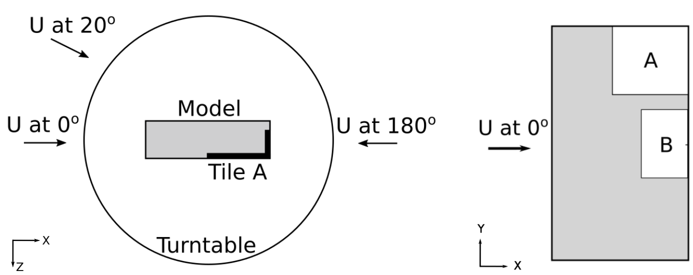

(a) Top view of the turntable, indicating the convention used for the wind direction (b) Side view of the building model

Figure 2: Sketch of the building model.

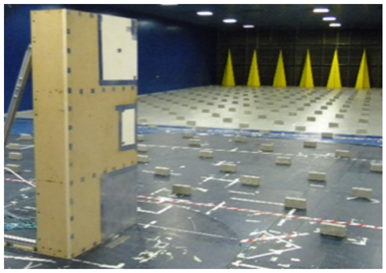

(a) PoliMi test section

(b) WoW test section

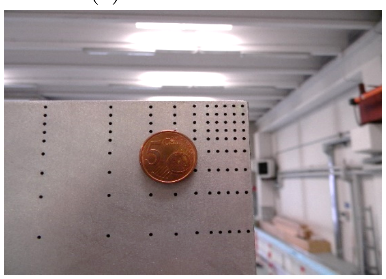

(c) pressure tap distribution on tile A

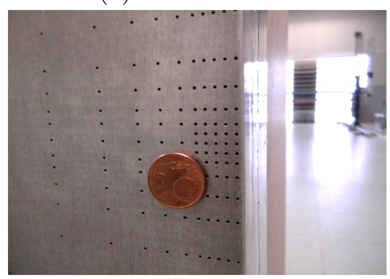

(d) pressure tap distribution on tile B

Figure 3: Pictures of the test sections of both wind tunnels and close-up of the aluminum tiles.

The experiment was designed to enable a detailed study of the pressure distribution in the regions of the building where the highest pressure peaks are expected, i.e. near the corners and edges of the building [17]. Therefore, we designed two aluminum tiles containing 224 and 223 pressure taps respectively: tile A located on the top-corner of the model and tile B centered at 1m height adjacent to the building edge (Figure 2). The minimum tap distance is 3.4mm on both tiles; the resolution is progressively decreased when moving away from the building edges. The pressure taps have an internal diameter of 1.3mm; they are connected to the pressure scanner system through rubber tubes with the same diameter to avoid discontinuities. Figure 3 shows the distribution of the pressure taps on tile A, together with the set-up of the experiment in the two wind tunnel facilities. The tubing system introduces distortion in the pressure signal; the raw pressure measurements are divided by the tubing frequency response function to account for this distortion and reconstruct the original pressure signal before post-processing.

2.2.2. Pressure Measurement System

At PoliMi, the model was instrumented with 7 PSI ESP-32 HD high-speed pressure scanners, connected to a data acquisition system with a sampling frequency of 500Hz. The outcome of each test consists of 300s time-series of pressure measured at 446 taps. The reference velocity of $\sim$ 11.8m/s at 2m height was measured during each test by a Pitot tube located 7m upwind of the building. The reference pressure was computed by pneumatically averaging the pressure recorded at 4 different points across the test section, during each test.

The WoW measurements were performed using pressure scanners with a sampling rate of 520Hz. As in the PoliMi wind tunnel, 300s time-series of pressure were recorded at 446 taps. The tests were performed at the same Reynolds number, i.e. with a target reference velocity of 11.8m/s at 2m height. At the beginning of the experiment, TFI Cobra probes were employed to measure the velocity at two vertical locations at a lateral distance of 2m from the building. Since the facility is an open-circuit wind tunnel, the reference pressure was determined from the nearest weather station. The details of both experiments are summarized in Table 2.

	$f_{samp}[Hz]$	$T[s]$	$U[m/s]$
PoliMi	500	300	11.7
WoW	520	300	11.0

Table 2: Sampling frequency, total duration and reference velocity at $2m$ height for the pressure measurements performed in both facilities.

3. Results

In this section, we first compare the velocity statistics of the incoming boundary layers generated in the two wind tunnels in terms of the mean velocity, turbulence intensities, integral time-scales, and velocity spectra. Non-dimensional quantities are presented, since the measurements were performed for different reference velocities. Subsequently, we present the comparison of the pressure measurements both in terms of statistics, i.e. mean, root mean square and spectra, and in terms of time-series and peak events. The pressure values are presented as non-dimensional C_p quantities defined as

$$C_p(t) = \frac{p(t) - p_{ref}}{\bar{q}_{ref}}, \tag{1}$$

where p_{ref} is the static reference pressure and $\bar{q}_{ref}$ is the average dynamic pressure measured at roof height.

From an engineering design point-of-view, surface pressure measurements are usually performed to assess the load on cladding elements and their supporting structure. The relevance of the peak phenomena is therefore determined by their effect on the area-averaged pressure acting on the panels. By exploiting the high density of pressure taps used in the experiments, we can compute the area-averaged pressure acting on a cladding element by direct numerical integration:

$$p_{AA}(t) = \frac{\sum p_i(t) A_i}{A_{tot}} \tag{2}$$

where p_{AA} is the area-averaged pressure on the panel, p_i is the pressure recorded by the i-th tap, A_i is the tributary area of the i-th tap, and A_{tot} is the total area of the panel (i.e. $A_{tot} = \sum A_i$). In the present paper we consider a typical panel size of $2 \times 3\text{m}^2$, although others may be employed. The resulting time signal can be analyzed using extreme value analysis techniques; in the present work, we employ the Cook & Mayne method [27].

3.1. Velocity statistics

In the following plots, the gray error-bars represent the variation of the velocity statistics measured at the different spanwise locations in the PoliMi wind tunnel, and the gray circles indicate the corresponding spanwise-averaged values; the red dots represent the data measured at WoW.

Figure 4 shows the profiles of mean streamwise velocity, nondimensionalized by the reference velocity at 2m height. The profiles are shown both in linear and logarithmic scale. The WoW measurements are within the spanwise variation of PoliMi data at all available measurement heights. When plotted in logarithmic scale, the velocity profiles manifest the expected linear trend of a neutral ABL.

By fitting regression lines to the data, we obtain a roughness length of $\sim$ 3mm and $\sim$ 2.5mm for the PoliMi and WoW tests respectively.

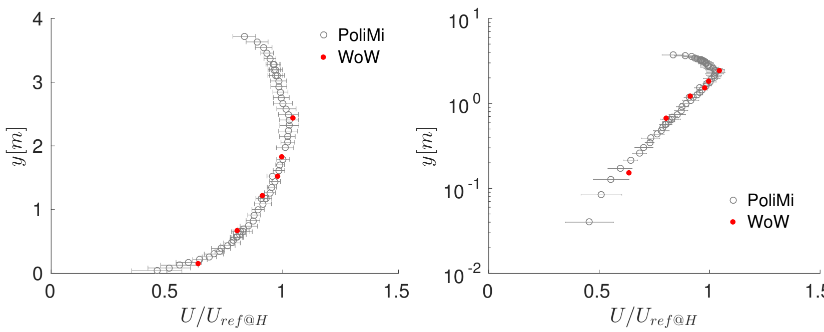

(a) linear-scale (b) log-scale

Figure 4: Comparison of nondimensional mean velocity between PoliMi and WoW data.

The turbulence intensities, defined as the ratio of the root mean square and the mean velocity, are compared in Figure 5. The streamwise turbulence intensity measured at WoW is within the interval defined by the spanwise variation in the PoliMi experiments, except for the lowest and highest points. The highest discrepancy occurs close to the ground where the turbulence intensity in WoW is ~ 0.07 lower than the PoliMi spanwise-averaged value. The WoW profiles of vertical turbulence intensity are ~ 0.06 lower close to the ground and ~ 0.02 higher above 1.8m. Similarly, the spanwise turbulence intensity computed from WoW data at 0.15m height is ~ 0.045 lower than PoliMi spanwise-averaged value at the same height and above 1.5m it is $\sim 0.02 - 0.03$ higher.

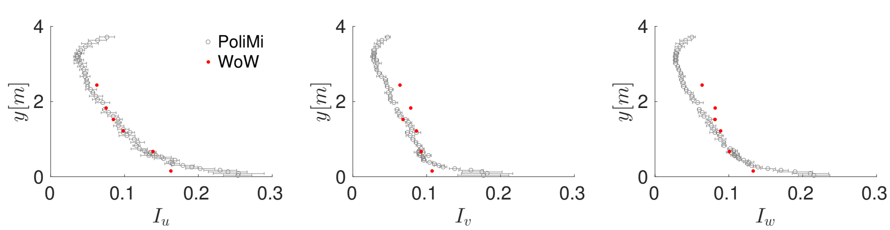

(a) streamwise turbulence intensity (b) vertical turbulence intensity (c) spanwise turbulence intensity

Figure 5: Comparison of turbulence intensities between PoliMi and WoW data.

Figure 6 shows the comparison in terms of non dimensional integral time-scales; the profiles are nondimensionalized using the reference velocity at roof height and the height of the building. All three components show reasonable agreement, considering that a significant spanwise variation is observed in the PoliMi experiment. The main discrepancy between the two datasets again appears close to the ground in the vertical and spanwise profiles.

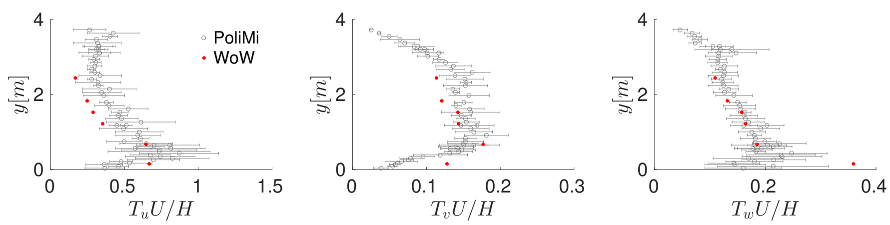

(a) streamwise time-scale (b) vertical time-scale (c) spanwise time-scale

Figure 6: Comparison of nondimensional integral time-scales between PoliMi and WoW data.

Finally, the power spectra of the streamwise velocity component are compared to the standard Von-Karman spectrum in Figure 7. The three profiles agree well throughout the range of nondimensional frequencies that the two experiments have in common. The longer time-series measured in the WoW test allow to capture larger scales compared to the PoliMi experiment; this is evident from the lower frequencies in the spectrum computed from the WoW data. Conversely, even though the sampling frequency of the cobra probes is higher than the sampling frequency of the hot-wires, the spectrum measured at PoliMi contains higher nondimensional frequencies compared to WoW data. This is a result of the fact that the Reynolds number of the WoW experiment is almost 5 times larger than the Reynolds number of the PoliMi test; therefore, the sampling frequency of 2500Hz does not enable the measurement of scales as small as in the PoliMi wind tunnel.

The comparison of the velocity statistics indicates that the PoliMi and WoW experimental set-ups have very similar incoming ABLs, both in terms of the time-averaged velocity and the turbulence quantities.

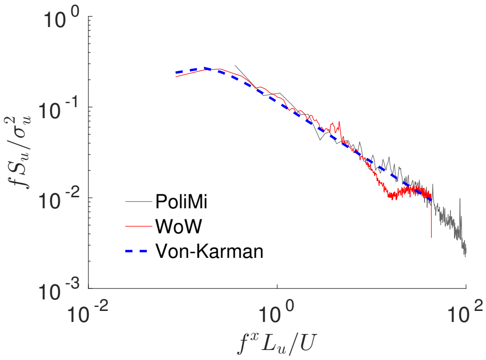

Figure 7: Comparison of streamwise velocity spectra between PoliMi and WoW data at 0.67m height, compared to the Von-Karman spectrum adapted for wind engineering [28]

.

3.2. Pressure statistics

In this section we first compare the pressure statistics measured in the two wind tunnels, for two configurations: $0-180°$ and $20°$ wind directions. Subsequently, we present the comparison of the time-series and peak valuesfor the $20°$ wind direction, which produced the strongest suction peaks [17].

3.2.1. $0-180°$ *wind directions*

Figure 8 shows the distribution of the pressure coefficient statistics on the building's lateral facade at $0-180°$ wind directions. The mean pressure coefficients recorded in both wind tunnels agree well qualitatively: the flow first separates at the windward edge generating an area of relatively strong negative pressure coefficient (red region in Figures 8a and 8b), then it reattaches on the rear part of the model (yellow region in Figures 8a and 8b). From the contour plot it appears that the WoW data experiences a slightly stronger negative pressure coefficient, especially in the separation region. The distribution of the root mean square (rms) of the pressure coefficient is shown in Figures 8c and 8d. Both sets of measurements show high fluctuations in the region of flow separation and reattachment; the rms C_p computed at WoW is slightly higher than the PoliMi one, especially in the separation region.

Figure 9 provides a more quantitative comparison, showing the statistics of

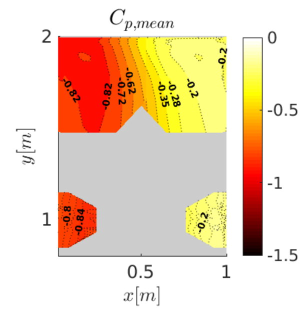

(a) PoliMi: mean pressure coefficient

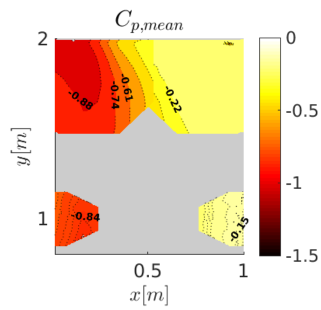

(b) WoW: mean pressure coefficient

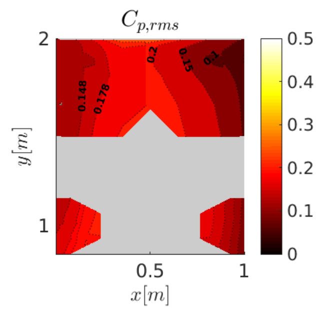

(c) PoliMi: rms pressure coefficient

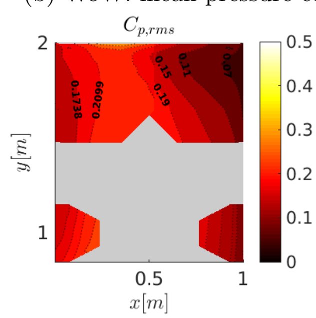

(d) WoW: rms pressure coefficient

Figure 8: Comparison of pressure coefficient first and second order statistics. Tiles on the right and on the left of each subplot refer to 0° and 180° wind directions respectively.

the pressure coefficient along two rows of taps on tiles A and B respectively. The highest discrepancy is experienced on the top part of the model (tile A) in the reattachment region. The maximum difference in the time-averaged pressure coefficient along the row of taps at 1.76m height, is ~ 0.19 (Figure 9b); the maximum difference in rms C_p is ~ 0.04 (Figure 9c). Along the row of taps at 1m (Figures 9f), the agreement between the two data-sets is rather good in both upwind and downwind locations. The maximum discrepancy in time-averaged and rms coefficients is ~ 0.05 and ~ 0.02 respectively.

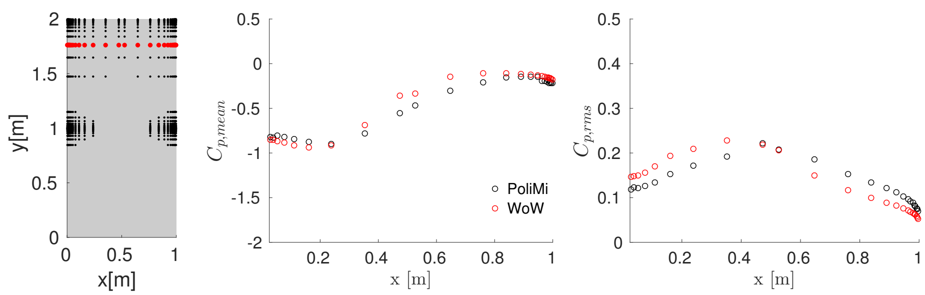

(a) Row of taps on tile A (b) Mean pressure coefficient on tile A (c) Root mean square pressure coefficient on tile A

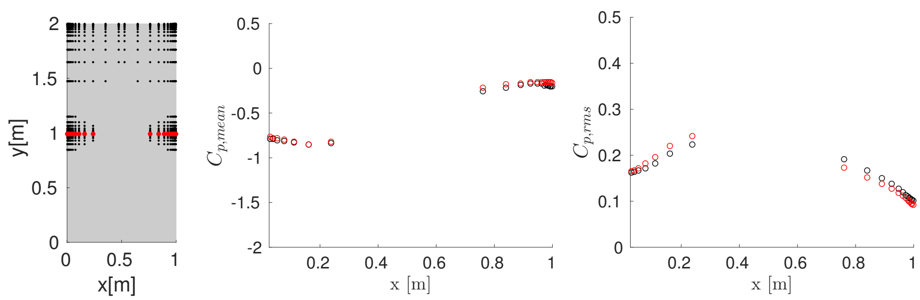

(d) Row of taps on tile B (e) Mean pressure coefficient on tile B (f) Root mean square pressure coefficient on tile B

Figure 9: Comparison of mean and root mean square pressure coefficients, at $0 - 180°$.

The difference between the two experiments could partially be explained by looking at the characteristics of the incoming boundary layers. While the mean velocity profiles agree well (Figure 4), the profiles of turbulence intensity manifest some discrepancies above 1.7m (Figure 5). The higher turbulence intensities generated at WoW could result in higher pressure fluctuations in the separation region, compared to the PoliMi experiment [29]. Furthermore, the higher turbulence intensities in the WoW experiment could cause the reattachment point of the flow to move upstream, resulting in faster recovery and lower absolute values of mean and fluctuating C_p in the rear portion of the model [29, 30].

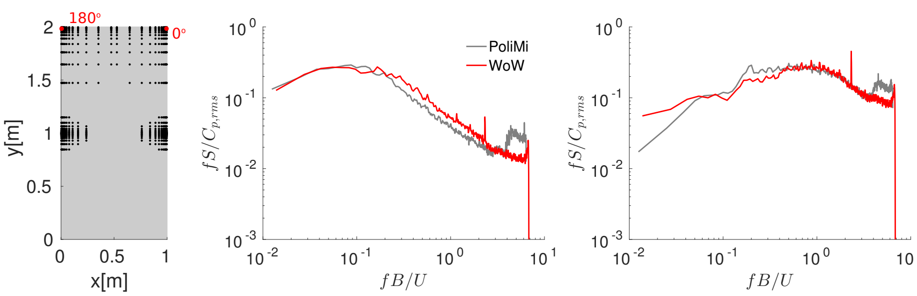

(a) Top-corner tap (b) power spectral density at 180° (c) power spectral density at 0°

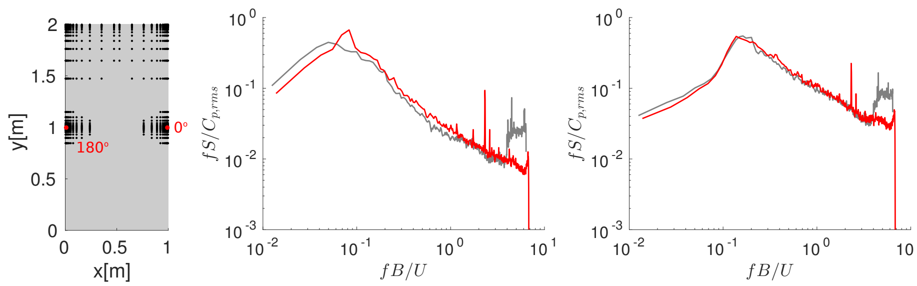

(d) Mid-edge tap (e) power spectral density at 180° (f) power spectral density at 0°

Figure 10: Non-dimensional power spectral density of the pressure coefficient at $0 - 180°$ wind direction on top-corner and mid-edge taps.

In Figure 10 we plot the power spectral density of the pressure coefficient measured in the same tap at 0° and 180° wind directions (marked by the red dots). The power spectra are adimensionalized using the frequency; the adimensional frequency is computed using the reference velocity at roof height and the width of the model (B). The comparison between the two experiments shows good agreement at most frequencies. Considering the top-corner tap (tile A), the only significant deviation appears at 0° at low frequencies, where WoW data reaches higher energy-content compared to PoliMi ones. Focusing on the pressure tap at 1m height (tile B), we can see that in both experiments the highest energy content occurs around $\frac{fB}{U} \sim 0.15$ and 0.08, at 180° (Figure 10e) and 0° (Figure 10f) respectively. The more local peaks observed at very high-frequencies are likely due to experimental noise.

3.2.2. 20° *wind direction*

Figure 11 shows the distribution of the mean and rms pressure coefficients on the building's lateral facade at 20° wind direction. In this configuration both tiles are located in the wake of the building and experience relatively strong suction and pressure fluctuations. The mean pressure coefficient measured at WoW appears slightly less strong than the PoliMi one (Figures 19a and 19b), while no significant differences in rms C_p are evident from Figures 11c and 11d.

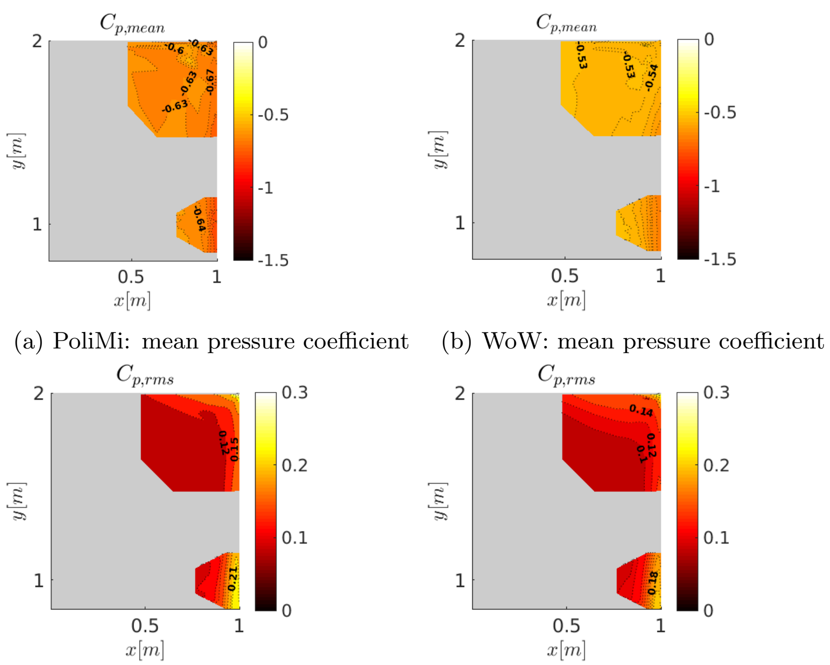

(a) PoliMi: mean pressure coefficient (b) WoW: mean pressure coefficient

(c) PoliMi: rms pressure coefficient (d) WoW: rms pressure coefficient

Figure 11: Comparison of mean and root mean square pressure coefficients, at 20° wind directions.

A quantitative comparison is again presented by considering two rows of taps along the building's lateral facade (Figure 12). The maximum discrepancy between the two data-sets along the row of taps selected on tile A is ~ 0.15

and ~ 0.02, for first and second order statistics respectively (Figures 12b and 12c); focusing on tile B, the difference in the mean and rms C_p is ~ 0.13 and ~ 0.03 respectively (Figures 12b and 12c). As for the $0-180°$ wind directions, these discrepancies could be caused by the differences in the boundary layer turbulence intensities.

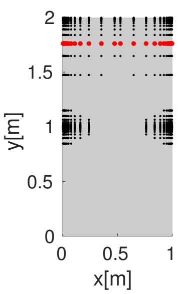

(a) Row of taps on tile A

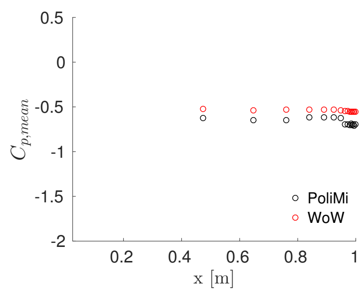

(b) Mean pressure coefficient on tile A

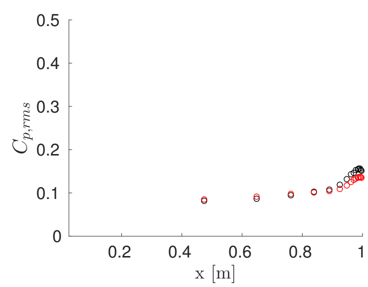

(c) Root mean square pressure coefficient on tile A

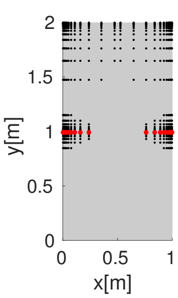

(d) Row of taps on tile A

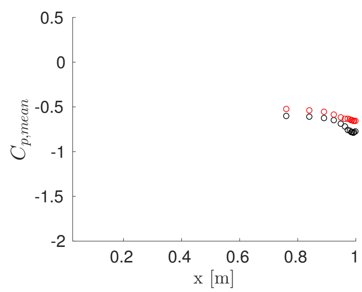

(e) Mean pressure coefficient on tile B

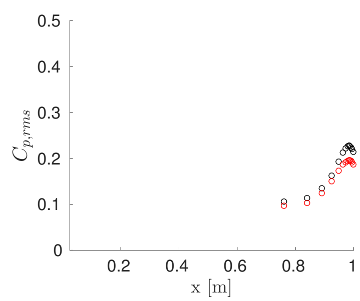

(f) Root mean square pressure coefficient on tile B

Figure 12: Comparison of pressure coefficient first and second order statistics, at 20°.

Figure 13 shows the power spectral density of the pressure coefficient measured in two taps (marked by the red dots) at 20° wind direction. The agreement between the two data-sets over the range of frequencies considered is good. When considering the pressure tap at 1m height, both experiments exhibit the highest energy content around $\frac{fB}{U} \sim 0.05$.

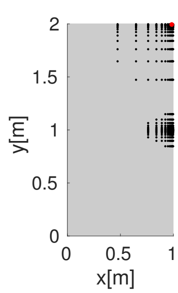

(a) Top-corner tap

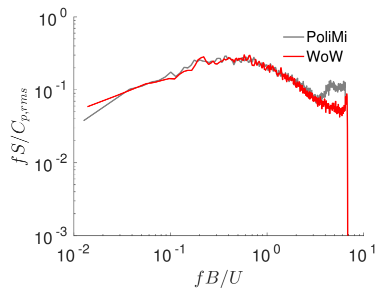

(b) power spectral density at 20°

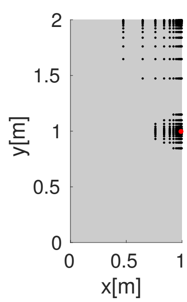

(c) Mid-edge tap

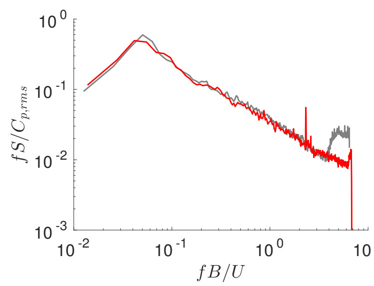

(d) power spectral density at 20°

Figure 13: Non-dimensional power spectral density of the pressure coefficient at 20° wind direction on top-corner and mid-edge taps.

3.3. Pressure peaks

The comparison in terms of pressure peaks focuses only on the 20° case, since this represents the most interesting and critical situation for the locations of interest [17]. We first compare the frequency and strength of the local suction events observed during the two experiments by considering the time-series and the probability distributions of the pressure coefficient measured at an individual pressure tap. Subsequently, we present the probability distributions of the area-averaged pressure coefficient, considering a typical cladding panel of $2 \times 3\mathrm{m}^2$. To support the interpretation of the results, snapshots of the pressure time-series surrounding two different negative peak events are visualized.

In Figure 14 we show the time-series of the pressure coefficients recorded on a pressure tap adjacent to the corner of tile A, at 20° wind direction.

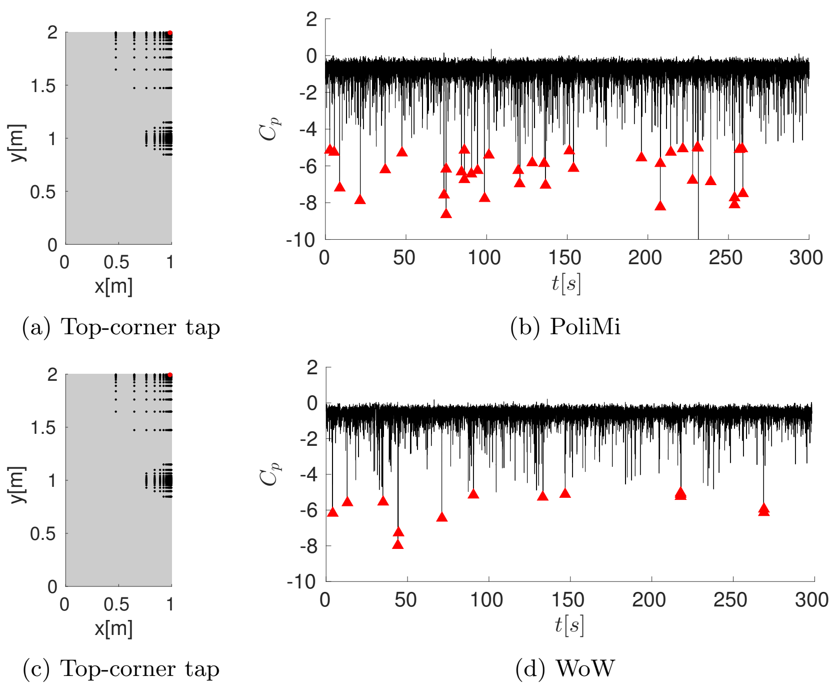

(a) Top-corner tap (b) PoliMi

(c) Top-corner tap (d) WoW

Figure 14: Time-series of pressure coefficient at 20° wind direction on top-corner tap. The red arrows indicate the negative peaks lower than $C_p = -5$

During the 300s period of the experiments, multiple negative peaks occur in both tests: 38 and 15 peaks stronger than $C_p = -5$ appear in the PoliMi and WoW time-series respectively (red arrows in Figure 14). The largest negative pressure coefficient recorded at PoliMi is ~ -10, while at WoW it is ~ -8. Qualitatively, the time-series exhibit very similar behavior, but the negative peak values measured at PoliMi are slightly stronger and more frequent than the WoW ones. Figure 15 shows the probability density functions (PDFs) of the pressure coefficients in both experiments on the same top-corner tap, and on a mid-edge tap on Tile B. The PDFs are shown both in linear and logarithmic scale. A similar non-Gaussian behavior is found: the distributions are significantly skewed to the left as a result of the negative pressure coefficient peaks. The plot in logarithmic scale highlights this asymmetry, with the left tail of the PDFs following a nearly linear trend. The effect is more pronounced on tile A than tile B; specifically the skewness of the PDFs on the top-corner tap is ~ -4.27 and ~ -4.35 for PoliMi and WoW data respectively (Figure 15b), while the corresponding values of skewness on the mid-edge tap are ~ -0.65 and ~ -0.69 (Figure 15e).

Figure 16 shows the PDFs of the pressure coefficient averaged over a $2 \times 3\text{m}^2$ cladding panel, highlighted in red in Figures 16a and 16d. The averaging operation filters out the most negative pressure coefficient peaks; as a result the PDFs manifest a less pronounced non-Gaussian behavior. The skewness of the PDFs on the top-corner panel is now reduced to ~ -1.11 and ~ -1.33 for PoliMi and WoW data respectively (Figure 16b), while the ones on the mid-edge panel are ~ -0.57 and ~ -0.58 (Figure 16e).

The high spatial resolution of the pressure taps enables further analysis of the spatial characteristics of the peak events to interpret the difference between the pdfs of the local and area-averaged pressure coefficients. Figure 17 depicts short time intervals around the occurrence of the peaks on the top-corner tap (Figures 17b and 17e) and the corresponding spatial distribution of the pressure coefficient at the time instants marked by the red arrows (Figures 17c and 17f). In addition, the pressure coefficient averaged over a $2 \times 3\text{m}^2$ panel (sketched in Figure 17c), is plotted during the same time period. In both experiments,

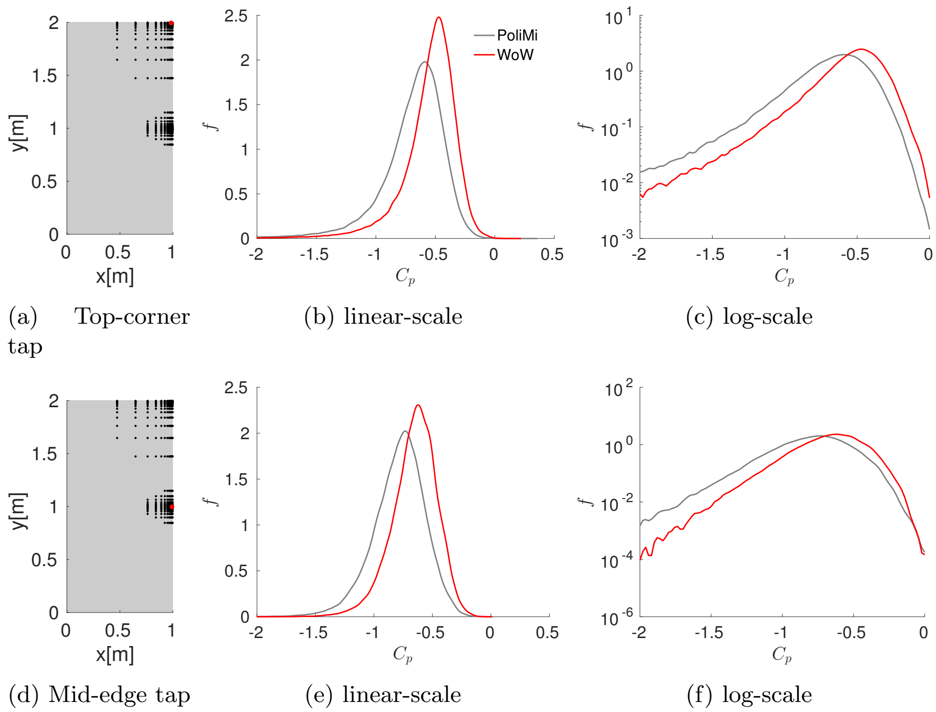

(a) Top-corner tap (b) linear-scale (c) log-scale

(d) Mid-edge tap (e) linear-scale (f) log-scale

Figure 15: Probability density functions of pressure coefficient at 20° wind direction.

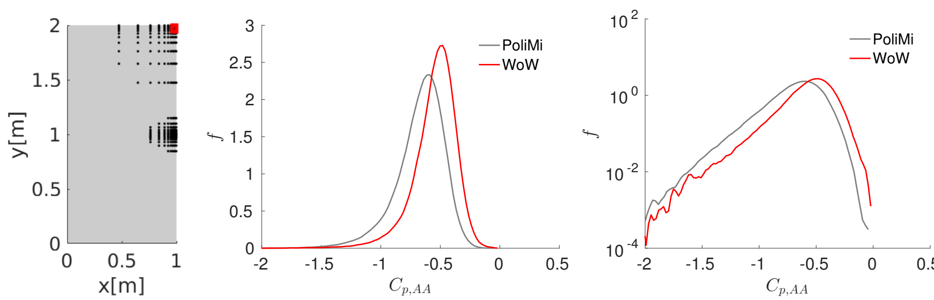

(a) Top-corner panel (b) linear-scale (c) log-scale

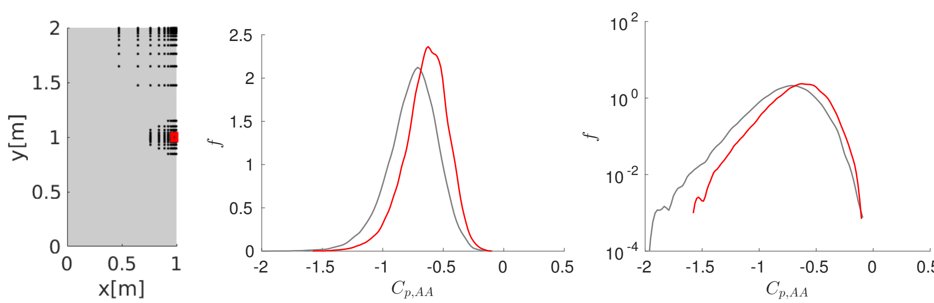

(d) Mid-edge panel (e) linear-scale (f) log-scale

Figure 16: Probability density functions of area-averaged pressure coefficient on $2 \times 3\text{m}^2$ panels, at 20° wind direction.

extremely concentrated peak events, both in time and space, are recorded in the same location, for the same wind direction. This type of events, which are limited in space and time, have a small effect on the area-averaged pressure, as evident from Figures 17b and 17e. Specifically, during the peak event observed at PoliMi, the area-averaged pressure coefficient drops below the mean value by ~ 0.7 for a period of time of ~ 34ms; at WoW a drop in area-averaged pressure coefficient of ~ 0.6 is observed for ~ 40ms. This type of event is not critical for the panel.

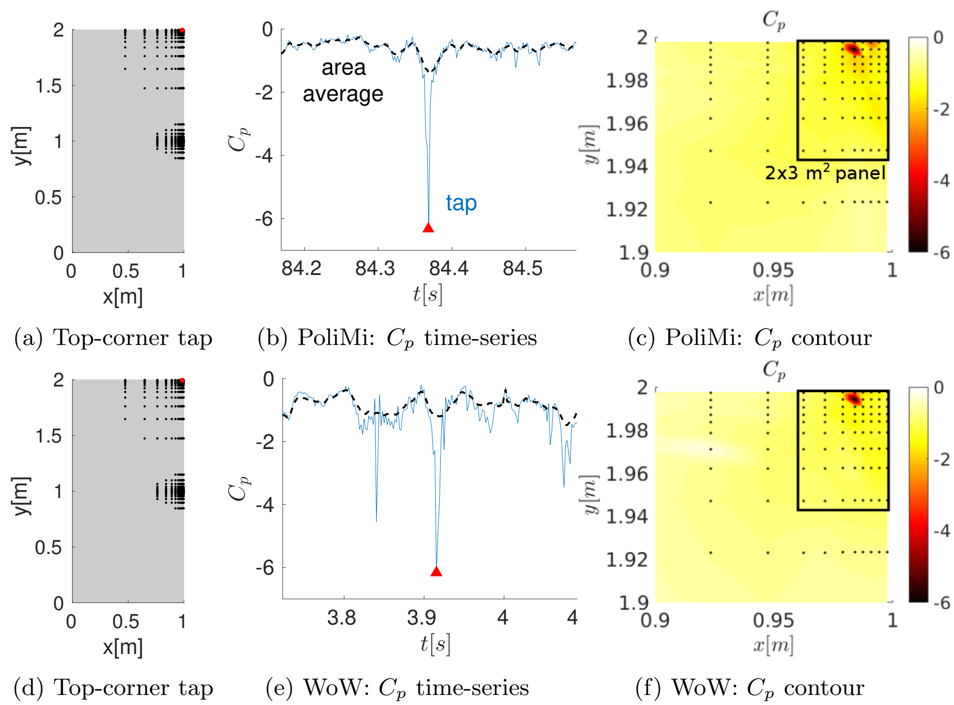

(a) Top-corner tap (b) PoliMi: C_p time-series (c) PoliMi: C_p contour

(d) Top-corner tap (e) WoW: C_p time-series (f) WoW: C_p contour

Figure 17: Time-series of pressure coefficient at 20° wind direction on top-corner tap, the red arrows indicate a negative peak lower than $C_p = -5$, and distribution of pressure coefficient around the tile at the time instant of the negative peak.

A completely different phenomenon can be observed during different time instants. Figure 18 depicts short time-series around the occurrence of pressure peaks at two nearby taps, indicated by the circles in the corresponding contour plots. The contour plots (Figures 18c and 18f) show the spatial distribution of the pressure coefficient at the time instants marked by the red arrows in the

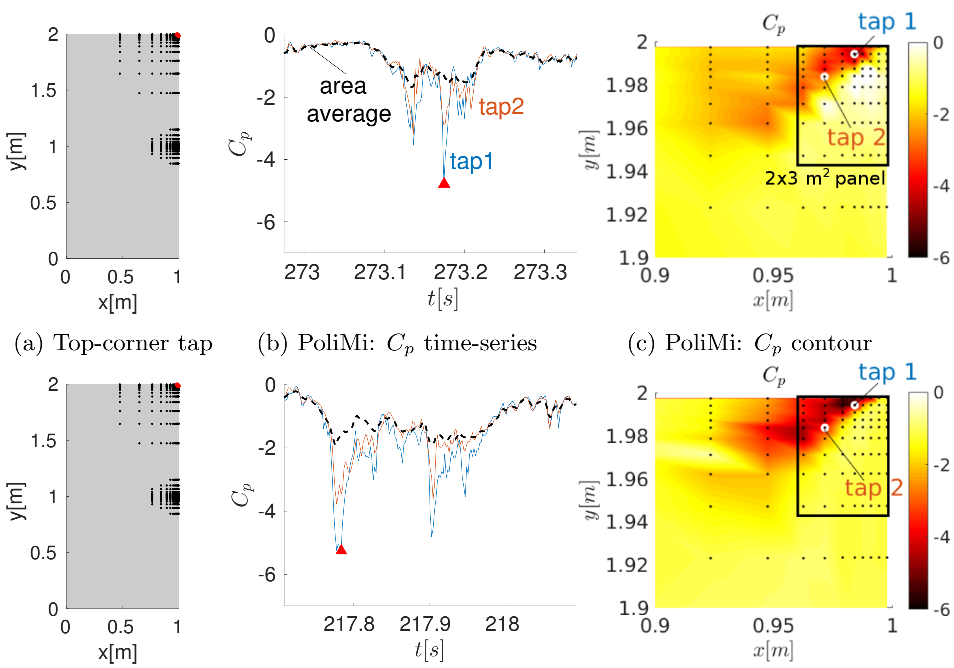

(a) Top-corner tap (b) PoliMi: C_p time-series (c) PoliMi: C_p contour

(d) Top-corner tap (e) WoW: C_p time-series (f) WoW: C_p contour

Figure 18: Time-series of pressure coefficient at 20° wind direction on top-corner tap, the red arrows indicate a negative peak lower than $C_p = -5$, and distribution of pressure coefficient around the tile at the time instant of the negative peak.

time-series (Figures 18b and 18e). In this case, both PoliMi and WoW tests experience a strong negative pressure coefficient, up to $C_p = -5$, that impacts a large portion of the tile. The time-series reveal that when the negative peak occurs in *tap 1*, *tap 2* experiences a negative peak at the same time, although weaker. This suction event extends for a longer time period than before, as evident from Figures 18b and 18e, and causes the area-averaged pressure to significantly deviate from the mean value. During the suction event measured at PoliMi, the area-averaged pressure coefficient drops below the mean value by ~ 1, for a period of time of ~ 120ms; at WoW a drop in area-averaged pressure coefficient of ~ 1.35 is observed for ~ 270ms.This phenomenon appears to be consistent between the two datasets, and represents a more critical situation than the sharp and concentrated peak of Figure 17.

3.4. Extreme value analysis

To compute the design pressure coefficients from the two datasets, we employ extreme value analysis both on the individual pressure taps and on the area-averaged value. In each case, the peak pressure coefficient is computed according to the Cook & Mayne method [27]: the time history of pressure coefficient is divided in windows, the most negative peak pressure coefficient is extracted from each window and a Gumbel distribution is fitted to the extreme values [14]. We used 16 windows of size 18s, equivalent to 6min in full-scale (assuming a full-scale reference velocity of 30m/s). Since the resulting windows are shorter than the recommended 10min window size, the Gumbel distribution is corrected according to the method proposed by Cook and Mayne [27]. Figure 19 shows the spatial distribution of the peak pressure coefficients with a 22% probability of exceedance adjacent to the top corner of the building's lateral facade. As expected, this region of the building experiences the highest negative values; here the sharp and strong suction events, such as the ones of Figure 17, cause the peak pressure coefficient to reach negative values below ~ -7. The spatial distribution is very similar between both experiments, but the PoliMi values are generally lower than those obtained from the WoW; this is consistent with the higher frequency and strength of the negative peak events observed in the time series.

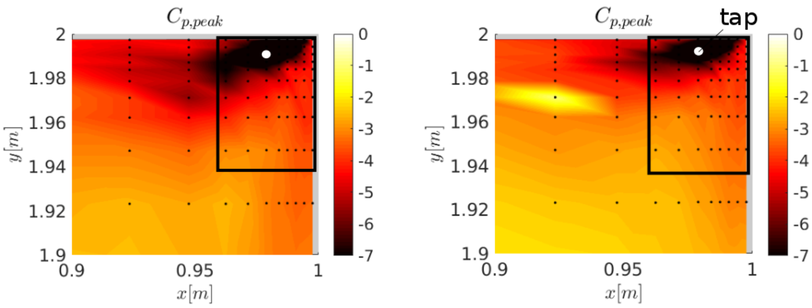

(a) PoliMi (b) WoW

Figure 19: Comparison of peak pressure coefficients relative to a 22% probability of exceedance, at 20° wind directions.

In terms of cladding design, the quantity of interest is the design pressure on the panels. Table 3 compares the design pressure coefficients relative to a 22% of exceedance and referenced to the dynamic pressure at roof height. We report both the local design pressure coefficients obtained from the single pressure tap indicated in Figure 19, and the values calculated for a $2 \times 3\text{m}^2$ panel, as sketched in Figure 19. The difference in the local values is 26%, but it reduces to only 10% when considering the area-averaged design pressure coefficient. This can be attributed to the localized effect of a subset of the strong suction events (Figure 17). As for the rms C_p, the differences in the design pressure coefficients obtained from both experiments could be related to the higher turbulence intensities that characterize the ABL at WoW. If the higher turbulence intensity causes the reattachment point of the flow on the side wall to move upstream, the flow will recover faster and could exhibit less strong and less frequent pressure fluctuations in the rear portion of the model [29, 30].

	PoliMi	WoW
Top-corner tap	-12.60	-9.37
Top-corner panel	-3.34	-3.01

Table 3: Peak pressure coefficient relative to a 22% probability of exceedance, 20° wind direction.

Finally, Figure 20b shows the decrease in the absolute value of the design pressure coefficient for panels of increasing dimension, keeping the aspect ratio constant to 1.5 (Figure 20a). The results show good agreement between both experiments: the maximum discrepancy is $\sim 10\%$. The design pressure coefficients calculated from the PoliMi test are consistently more negative than the WoW values, which is a consequence of the more frequent and stronger suction events.

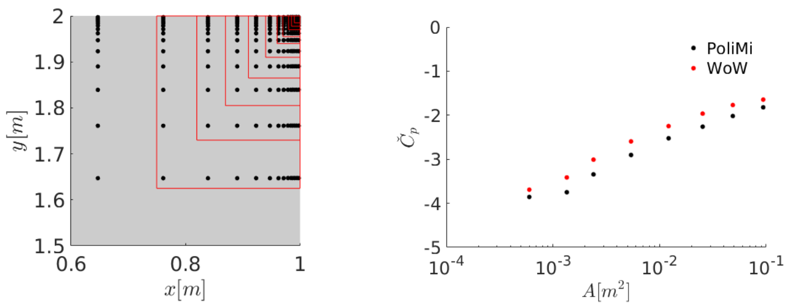

(a) Panels (b) Design pressure coefficient

Figure 20: Design pressure coefficient for panels of increasing area, 20° wind direction..

4. Conclusions and future work

In the present work, we presented high-resolution pressure measurements on a high-rise building model acquired in two different wind tunnels: the closed-circuit wind tunnel of Politecnico di Milano and the Wall of Wind open-circuit wind tunnel of Florida International University. The experiment was designed to enable detailed analysis of the nature of the pressure peaks that occur on the building's lateral facade [17]. The objective of the paper was to present the experimental set-up and the high-resolution pressure data, and to study the occurrence of peak events at individual pressure taps and their relation to the area-averaged pressure on a typical cladding panel size.

First, we presented a comparison of the velocity statistics of the two atmospheric boundary layers. The mean velocity data recorded at WoW is within the interval defined by the spanwise variation of the PoliMi measurements over the entire building height. The turbulence intensities and integral time-scales exhibit some differences close the ground and near the top of the building, but these differences are limited to a maximum discrepancy of 0.07 in turbulence intensity near the ground. Comparison of the power spectra of the streamwise velocity component further confirms good agreement between the atmospheric boundary layers generated in both experiments.

Subsequently, we compared the distributions of the mean and root mean square pressure coefficients on the building's lateral facade at $0-180^{\circ}$ and 20° wind directions. The two datasets show similar behavior; however, the negative pressure coefficient measured at WoW is slightly stronger than the one measured at PoliMi, especially in the separation region. Quantitative comparison of pressure coefficient profiles along two rows of taps indicates that the largest discrepancies in the mean and root mean square pressure coefficients (0.19 and 0.04 respectively) occur near the top of the building at $0-180^{\circ}$. The pressure power spectra for different pressure taps and at different wind directions indicate good agreement between both experiments.

Comparison of the pressure time-series recorded for the 20° wind direction shows frequent suction peaks in both experiments, resulting in a high skewness of the probability density functions of the pressure coefficients recorded at individual pressure taps. Both experiments reveal the occurrence of two types of pressure peak events: some peak events near the top corner of the building on tile A are very localized in space and time, while other events extend over a larger portion of the facade on both tile A and B. As a result, area-averaging of the pressure measurements decreases the skewness of the probability density functions for the pressure coefficient, and the design pressure coefficients for panels of increasing size decrease in absolute value. These effects are similar between both experiments, but the WoW values for the design pressure coefficients are consistently more negative than those from PoliMi, with a maximum discrepancy of 10% for a $2 \times 3\text{m}^2$ panel.

The observed discrepancies in the statistics of the pressure measurements obtained from the WoW and PoliMi experiments could be attributed to differences in the turbulence intensities of the boundary layers in both facilities. To further investigate this effect, future work will analyze additional tests performed at the WoW for higher Reynolds numbers and a different terrain exposure. In addition, future work will consider quantitative analysis of the space-time characteristics of the pressure signals to provide further insight on the relevance of the two types of suction events for cladding design. Finally, both data sets presented in this paper are made available to the scientific community to serve as a benchmark test case for numerical simulations and measurements of wind loads on high-rise buildings [24, 25].

5. Acknowledgements

The experimental design and the first experiment at PoliMi were supported by ARUP. The repeat experiment at WoW was supported by the National Science Foundation under Grant Number 1635137. We gratefully acknowledge the contribution of the staff at the NHERI Wall of Wind facility who made the WoW experiments possible. In particular, we wish to thank Walter Conklin, Arindam Chowdhury, Peter Irwin, Ashkan Rasouli and Maryam Refan.

[1] D Surry and T Stathopoulos. An experimental approach to the economical measurement of spatially-averaged wind loads. *Journal of Wind Engineering and Industrial Aerodynamics*, 2(4):385–397, 1978.

[2] WH Melbourne. Comparison of measurements on the caarc standard tall building model in simulated model wind flows. *Journal of Wind Engineering and Industrial Aerodynamics*, 6(1-2):73–88, 1980.

[3] JD Holmes. Distribution of peak wind loads on a low-rise building. *Journal of Wind Engineering and Industrial Aerodynamics*, 29(1-3):59–67, 1988.

[4] J E Cermak. Wind-tunnel development and trends in applications to civil engineering. *Journal of wind engineering and industrial aerodynamics*, 91(3):355–370, 2003.

[5] F Cluni, V Gusella, SMJ Spence, and G Bartoli. Wind action on regular and irregular tall buildings: Higher order moment statistical analysis by hffb and smpss measurements. *Journal of Wind Engineering and Industrial Aerodynamics*, 99(6-7):682–690, 2011.

[6] W Kim, Y Tamura, and A Yoshida. Interference effects on local peak pressures between two buildings. *Journal of Wind Engineering and Industrial Aerodynamics*, 99(5):584–600, 2011.

[7] MF Huang, W Lou, C M Chan, N Lin, and X Pan. Peak distributions and peak factors of wind-induced pressure processes on tall buildings. *Journal of Engineering Mechanics*, 139(12):1744–1756, 2013.

[8] JW Zhang and QS Li. Field measurements of wind pressures on a 600 m high skyscraper during a landfall typhoon and comparison with wind tunnel test. *Journal of Wind Engineering and Industrial Aerodynamics*, 175:391–407, 2018.

[9] Jon A Peterka and Jack E Cermak. Wind pressures on buildings-probability densities. *Journal of the structural division*, 101(6):1255–1267, 1975.

[10] JD Holmes. Non-gaussian characteristics of wind pressure fluctuations. *Journal of Wind Engineering and Industrial Aerodynamics*, 7(1):103–108, 1981.

[11] D Surry and D Djakovich. Fluctuating pressures on models of tall buildings. *Journal of wind engineering and industrial aerodynamics*, 58(1-2):81–112, 1995.

[12] Dae Kun Kwon and Ahsan Kareem. Peak factors for non-gaussian load effects revisited. *Journal of Structural Engineering*, 137(12):1611–1619, 2011.

[13] Fahim Sadek and Emil Simiu. Peak non-gaussian wind effects for database-assisted low-rise building design. *Journal of Engineering Mechanics*, 128(5):530–539, 2002.

[14] Xinlai Peng, Luping Yang, Eri Gavanski, Kurtis Gurley, and David Prevatt. A comparison of methods to estimate peak wind loads on buildings. *Journal of wind engineering and industrial aerodynamics*, 126:11–23, 2014.

[15] Nicholas J Cook. on the gaussian-exponential mixture model for pressure coefficients. *Journal of Wind Engineering and Industrial Aerodynamics*, 153:71–77, 2016.

[16] D Rocchi, P Schito, and A Zasso. Investigation on the relation between incoming wind characteristics and surface pressure distribution. *Journal of Wind Engineering and Industrial Aerodynamics*, 2011.

[17] L Amerio. *Experimental high resolution analysis of the pressure peaks on a building scale model facades*. PhD thesis, Italy, 2018.

[18] J-X Lin, D Surry, and HW Tieleman. The distribution of pressure near roof corners of flat roof low buildings. *Journal of wind engineering and industrial aerodynamics*, 56(2-3):235–265, 1995.

[19] D Banks, RN Meroney, PP Sarkar, Z Zhao, and F Wu. Flow visualization of conical vortices on flat roofs with simultaneous surface pressure measurement. *Journal of Wind Engineering and Industrial Aerodynamics*, 84(1):65–85, 2000.

[20] F Wu, PP Sarkar, KC Mehta, and Z Zhao. Influence of incident wind turbulence on pressure fluctuations near flat-roof corners. *Journal of Wind Engineering and Industrial Aerodynamics*, 89(5):403–420, 2001.

[21] X Peng, L Yang, E Gavanski, K Gurley, and D Prevatt. A comparison of methods to estimate peak wind loads on buildings. *Journal of wind engineering and industrial aerodynamics*, 126:11–23, 2014.

[22] E Gavanski and Y Uematsu. Local wind pressures acting on walls of low-rise buildings and comparisons to the japanese and us wind loading provisions. *Journal of Wind Engineering and Industrial Aerodynamics*, 132:77–91, 2014.

[23] P Huang, X Peng, and M Gu. Aerodynamic devices to mitigate rooftop suctions on a gable roof building. *Journal of wind engineering and industrial aerodynamics*, 135:90–104, 2014.

[24] OpenAIRE. Zenodo. https://zenodo.org, 2019.

[25] Stanford University. Stanford digital repository. https://library.stanford.edu/research/stanford-digital-repository, 2019.

[26] L Amerio, G Lamberti, G Pomaranzi, A Zasso, and C Gorlé. Comparison of high-resolution pressure peaks in closed and open-section wind tunnels. *Italian conference on wind engineering (INVENTO)*, 2018.

[27] NJ Cook and JR Mayne. A novel working approach to the assessment of wind loads for equivalent static design. *Journal of Wind Engineering and Industrial Aerodynamics*, 4(2):149–164, 1979.

[28] R. Harris. On the spectrum and auto-correlation function of gustiness in high winds. *Electrical Research Association*, 1968.

[29] PJ Saathoff and WH Melbourne. The generation of peak pressures in separated/reattaching flows. *Journal of Wind Engineering and Industrial Aerodynamics*, 32(1-2):121–134, 1989.

[30] John D Holmes. *Wind loading of structures*. CRC press, 2018.